

## ChemComm

## In operando Raman Microscopy of Cu/Li1.5Al0.5Ge1.5(PO4)3 Solid Electrolyte Interphase

Journal:	ChemComm
Manuscript ID	CC-COM-10-2024-005718.R1
Article Type:	Communication

SCHOLARONE™ Manuscripts

### COMMUNICATION

# *In operando* Raman Microscopy of Cu/Li<sub>1.5</sub>Al<sub>0.5</sub>Ge<sub>1.5</sub>(PO<sub>4</sub>)<sub>3</sub> Solid Electrolyte Interphase

Ineke Weich<sup>a</sup>, Andrew Dopilka<sup>b</sup>, Johannes Kasnatscheew<sup>a</sup>, Martin Winter<sup>a,c</sup>, Robert Kostecki<sup>b\*</sup>

Received 00th January 20xx, Accepted 00th January 20xx

DOI: 10.1039/x0xx00000x

Li<sub>1.5</sub>Al<sub>0.5</sub>Ge<sub>1.5</sub>(PO<sub>4</sub>)<sub>3</sub> (LAGP) is a promising solid-state electrolyte (SSE) for solid-state batteries due to its high Li<sup>+</sup> conductivity, wide operating potential window and moisture stability. However, LAGP electrolyte suffers from side reactions with Li metal resulting in thin-film formation, cracking and interfacial resistance rise which hinder its practical application. In this study, *in operando* Raman spectroscopy was performed to gain insights into local, potential dependent chemical and structural transformations of the Cu/LAGP interface during cathodic polarization.

Solid-state lithium batteries (SSLB) are considered the next generation battery technology, mainly because of higher energy density than conventional Li-ion batteries. Also, SSLB are safer because they are non-flammable and not prone to leaking liquid electrolyte. The use of a SSE can enable the commercial-scale application of the Li metal anode, improve cycle life, and extend the operating temperature range of the battery. Furthermore, the absence of liquid electrolyte can enable the bipolar electrode stack architecture, which can further enhance the cell energy density by increasing the ratio of active to inactive materials. 6.7

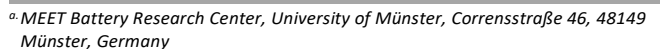
A class of commonly investigated SSEs for Li metal solid-state batteries are sodium super ionic conductor (NASICON)-structured derived phosphate-based electrolytes. Li<sub>1.5</sub>Al<sub>0.5</sub>Ge<sub>1.5</sub>(PO<sub>4</sub>)<sub>3</sub> (LAGP),<sup>8,9</sup> in particular, is a widely studied electrolyte for solid-state batteries because of its high ionic conductivity ( $\sim$ 0.1-1 mS cm<sup>-1</sup> at 25°C<sup>10</sup>) and excellent moisture stability.<sup>11</sup> Furthermore, LAGP has one of the highest calculated (4.27 V vs. Li|Li<sup>+</sup>)<sup>4,12</sup> and reported (6 – 7 V vs Li|Li<sup>+</sup>) anodic potential stability limit amongst oxide SSEs, which makes it compatible with high voltage cathodes.<sup>13</sup>

LAGP's poor cathodic stability (calculated at 2.70 V<sup>12</sup>) represents a major hurdle for practical solid-state battery applications. The electrochemical or chemical reduction of LAGP by direct contact with Li metal leads to the formation of a mixed conductor interphase (MCI).<sup>8,14–16</sup> Since the MCI conducts both ions and electrons, it allows for the continuous decomposition of the electrolyte, leading to local volume expansion mechanical failure

and cracking of the SSE during long-term cycling.  $^{17}$  It is assumed that the interphase formed through the chemical reduction of  $^{4+}$  results in a mixture of LAGP of various stoichiometries and lithiated oxides.  $^{13,18,19}$  Chung et al.  $^{19}$  reported that the direct contact of Li metal and LAGP leads to formation of  $\text{Li}_2\text{O}$ ,  $\text{Li}_2\text{O}_2$ , and  $\text{Li}_2\text{CO}_3$ . Feng et al. speculated that the LAGP is reduced to  $\text{Ge}^0$  particles which are embedded in  $\text{Li}_3\text{PO}_4$  and  $\text{AlPO}_4$  matrix. Based on first-principles calculations Zhu et al.  $^{12}$  predicted reduction products such as  $\text{Ge}^0$ ,  $\text{GeO}_2$ ,  $\text{Li}_4\text{P}_2\text{O}_7$ , and  $\text{AlPO}_4$ . In operando XPS study of LAGP electrochemical reduction on a graphene electrode showed that  $\text{Ge}^{4+}$  was converted to  $\text{Ge}^0$  after a voltage hold at 0.5 V.  $^{20}$ . However, there are still open questions about the local phase composition and distribution, and the large discrepancy between experimental and calculated cathodic stability potential limit.

Sang et al. successfully analysed SSE/electrode interfaces and their chemical changes using *in operando* Raman spectroscopy, employing gold thin-film as the electrical conductor and optical window for the Raman probe.<sup>21</sup> They followed up their investigations by studying the effect of interlayers (Si and LiAlO) at thiophosphate solid electrolyte/gold interfaces, demonstrating the applicability of *in operando* Raman spectroscopy to study SSEs.<sup>22</sup>

To gain further insight into LAGP's interfacial reactions mechanism, we conduct *in operando* Raman microscopy of the Cu/LAGP interface as the function of potential and location. Raman microscopy is well suited because of its relatively high spatial resolution (~1  $\mu$ m), non-destructive nature and compatibility with various experimental environments. Furthermore, the technique is highly sensitive to the vibrational modes of the PO<sub>4</sub> tetrahedron in the NASICON structure<sup>10,23,24</sup> along with spectral signatures of its decomposition products (Ge, GeO<sub>2</sub>, AlPO<sub>4</sub>).



b. Energy Storage and Distributed Resources Division, Lawrence Berkeley National Laboratory, Berkeley, California 94720, United States

Supplementary Information available: Additional information about the in materials and method, operando cell, supplemental XPS and AFM data are provided. See DOI: 10.1039/x0xx00000x

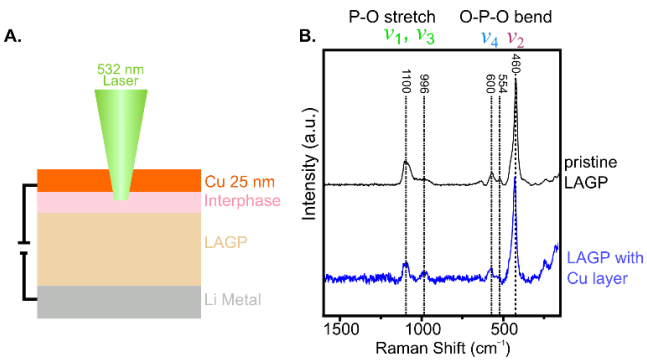


**Figure 1:** A. Schematic of the Raman *in operando* experiment. B. Raman spectra of pristine LAGP and LAGP coated with 25 nm Cu layer.

<sup>&</sup>lt;sup>c</sup> Helmholtz-Institute Münster, IEK-12, Forschungszentrum Jülich GmbH, Corrensstraße 48, 48149 Münster, Germany

<sup>\*</sup>r kostecki@lbl.aov

ARTICLE Journal Name

**Figure 1A** shows a schematic of the *in operando* Raman experimental setup to probe the Cu/LAGP interface. The Cu 25 nm thin-film serves as the current collector and optical window for the Raman laser probe.<sup>25</sup> In fact, Raman spectra of the bare LAGP surface and the LAGP coated with 25 nm Cu layer (**Figure 1B**) look nearly identical, contrary to the corresponding X-ray photoelectron spectra (**Figure S1**) where the signal from LAGP was almost completely attenuated by the Cu thin-film.

The crystal structure of LAGP consists of  $MO_6$  (M= Ge, Al) octahedra which are corner sharing with  $PO_4$  tetrahedra and Li<sup>+</sup> in the interstitial spaces. The Raman spectrum of the pristine LAGP is dominated by the vibrational modes of the  $PO_4$  tetrahedra and matches well with the previously reported spectra.  $^{10,23}$  The peak at  $^{460}$  cm $^{-1}$  corresponds to the symmetric ( $v_2$ ) bending mode of  $PO_4$  whereas the peaks in 550-600 cm $^{-1}$  range are assigned to O-P-O antisymmetric ( $v_4$ ) bending (marked in purple and blue in **Figure 1B**, respectively). The higher energy antisymmetric ( $v_3$ ) and symmetric ( $v_1$ ) stretching modes are at 996 and 1100 cm $^{-1}$  (marked green in **Figure 1B**). During the *in operando* measurements we tracked the intensity of the P-O stretching band at 1100 cm $^{-1}$  and the O-P-O symmetric bending mode at 460 cm $^{-1}$ .

Figure 2 shows a cyclic voltammogram (CV) of the 25 nm Cu thin-film working electrode in contact with LAGP electrolyte recorded in the spectro-electrochemical cell equipped with Li-foil counter electrode (Figure S2). The cathodic scan consists of a small peak at 1.5 V followed by a steady increase of the cathodic current with a threshold at ~0.85 V. This is consistent with the previously reported results, indicating the non-passivating character of the corresponding reactions. <sup>13,20,26</sup> Notably, the small cathodic peak at 1.7 V was also observed by Zallocco et. al. but its origin was not determined. <sup>26</sup> During the anodic scan, there is a quite pronounced peak at 0.55 V followed by a small one at 1.0 V. The excess of cathodic charge (88.5%) consumed during the CV scan correspond to irreversible electroreduction of LAGP at potentials <0.85 V.

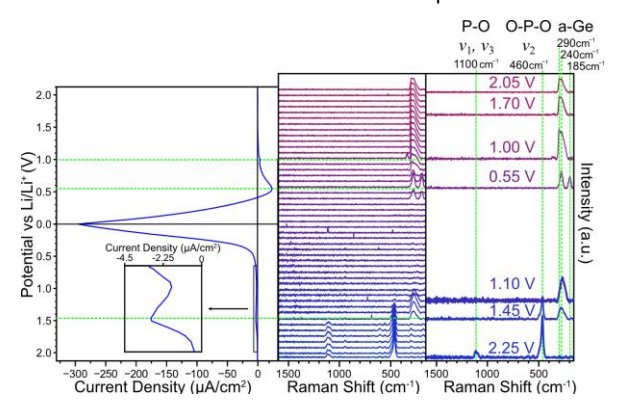


**Figure 2:** CV scan of the Cu/LAGP/Li cell at a scanning rate of 0.1 mV/s and *in operando* Raman spectra (selected spectra are shown on the right).

To monitor chemical and structural changes at the Cu/LAGP interface during potential polarization, Raman spectra were collected over the course of the CV scan (**Figure 2**). The stretching and bending modes of the PO<sub>4</sub> at 1100 cm<sup>-1</sup> and 460 cm<sup>-1</sup> are clearly visible in the spectra collected at open circuit potential. As the cathodic scan progresses, a steady decrease in intensity of the LAGP-related peaks begins at ca. 1.45 V together with an emergence of a new band at 290 cm<sup>-1</sup>, which is assigned to the phonon modes of amorphous Ge (a-Ge).<sup>27</sup> At 1.1 V, the LAGP peaks become undetectable, while the a-Ge peak persists until 1.0 V.

During the anodic scan, new peaks at 240 cm<sup>-1</sup> and 185 cm<sup>-1</sup> are

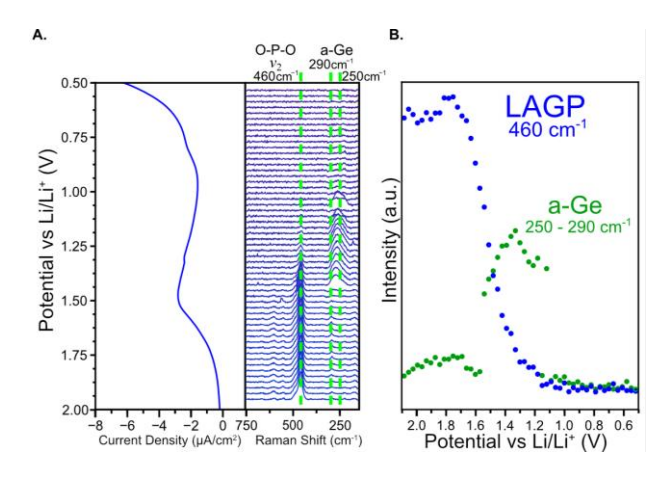


**Figure 3: A.** in operando Raman spectra of the Cu/LAGP interface during the initial cathodic CV scan at 0.1 mV/s. **B.** Progression of the intensities of 460 cm $^{-1}$  (LAGP) and 250-290 cm $^{-1}$  (a-Ge) bands as a function of the voltage 2.1 – 1.2 V.

observed from 0.35 V onwards, which could be attributed to  $\text{Li}_x\text{Ge}$  intermetallic compounds. Miao et al. showed that  $\text{Li}_{15}\text{Ge}_4$  is characterized by two bands at 240 cm<sup>-1</sup> and 450 cm<sup>-1</sup>. <sup>27</sup> Loaiza et al. observed a peak at 220 cm<sup>-1</sup> which was attributed to  $\text{Li}_x\text{Ge}$  phase. <sup>28</sup> However, these Li-rich crystalline or amorphous Ge phases are likely to be weak Raman scatterers and difficult to be observe. Delithiation of  $\text{Li}_x\text{Ge}$  starts around 0.6 V, leading to the formation of a-Ge and increase in the corresponding peak at 290 cm<sup>-1</sup>.

Since LAGP-related peaks do not reappear during the anodic scan, it can be assumed that the reduction from Ge<sup>4+</sup> in the LAGP to a-Ge (Ge<sup>0</sup>) is irreversible and that the subsequent interfacial reactions primarily occur at a-Ge which is further reduced to Li<sub>x</sub>Ge phases. Feng et al. hypothesized about the possibility of irreversible reduction of LAGP to a-Ge and the reversible lithiation/delithiation reaction of a-Ge.<sup>13</sup> Furthermore, Hartmann et al. analysed the formation of MCI on SSE using *in operando* XPS and showing that the Ge 3d line is shifted to elementary Ge and the signal of Ge ion is reduced, which is consistent with our observations.<sup>8,20</sup>

Ex situ XPS depth profiling of the Cu/LAGP after the single CV cycle to confirm the reduction of the Ge. **Figure S3** shows that after two initial etching cycles to remove the Cu layer, the Ge 2p line reveals peaks at 1219.34 and 1217.13 eV corresponding to Ge<sup>0</sup> and Ge<sup>-1</sup>, Ge<sup>-2</sup> from Li<sub>x</sub>Ge phases. More etching resulted in an emergence of the (Ge<sup>4+</sup>) peak at 1221.80 eV, which matches well with the pristine LAGP, indicating that the resulting LAGP decomposition was constrained to the surface region near the Cu/LAGP interface rather than extending into the deep into the bulk electrolyte.

The vibrational modes corresponding to LAGP disappear at 1.1 V, suggesting the initial  $Ge^{4+} \rightarrow Ge^{0}$  reaction occurs prior to the increase in cathodic current at 0.85 V. **Figure 3** shows an exploded view of the cathodic current and Raman spectra between 2.0 and 0.5 V. The evolution of the LAGP and a-Ge band intensity in this voltage region is shown in **Figure 3B**. The gradual increase in the a-Ge peak at 290 cm<sup>-1</sup> is coupled with steady decrease in the intensity of the LAGP band at 460 cm<sup>-1</sup>. From 1.2 V, the a-Ge peak decreases due to the conversion of a-Ge to Li<sub>x</sub>Ge, which disrupts the phonon modes of Ge by breakage of Ge-Ge bonds.

This onset potential 1.6 V for electroreduction of  $Ge^{4+}$  to a-Ge is consistent with literature data regarding the electrochemical reduction of  $GeO_2$  to  $Ge^0$  showing cathodic current onsets around  $1.0-1.5\ V.^{29,30}$  In addition, the theoretically calculated cathodic potential stability limit for LAGP is reported to be 2.70 V with predicted reduction products of Ge,  $GeO_2$ ,  $Li_4P_2O_7$  and  $AIPO_4$ . The

Journal Name ARTICLE

observed lower LAGP electroreduction onset potential compared to theoretically predicted demonstrates the large overpotential to decompose LAGP, a common phenomenon amongst SSEs.  $^{12}$  Interestingly, the electroreduction of LAGP at  $1.6-1.2\ V$  appears to be a passivating reaction and/or diffusion controlled process. This suggests that the initial LAGP reduction to a-Ge does not form an MCI but is followed directly by lithiation of the Ge to Li\_xGe phases, which create an MCI at lower potentials ca.  $0.85\ V$ , resulting in a monotonic increase in cathodic current with voltage.

Another noticeable observation is the lack of modes related to P-O vibrations below 1.1 V. Initially, the Raman spectra are dominated by strong bands associated with P-O stretching and O-P-O bending from the LAGP PO $_4$  tetrahedra. Once the LAGP gets reduced to a-Ge, the lattice phonon mode of Ge become visible but there is no trace of spectral features characteristic to other alleged decomposition products i.e., Li $_2$ O, Li $_2$ O $_2$ , GeO $_2$ , Li $_4$ P $_2$ O $_7$ , and AlPO $_4$  which are all Raman active.

To explore spatial heterogeneity of LAGP decomposition products at the initial stages of electroreduction, we performed Raman mapping of the Cu/LAGP interface over an area of  $40 \times 40 \mu m$  at  $2.3 \mu m$  resolution during the initial cathodic scan from 2.24 to 0.8 V. Figure 4A&B shows the current-voltage profile between 2.24 and 0.8 V and average Raman spectra of the images recorded at each potential. At 2.24 V, the average Raman spectrum matches well the single point spectrum of pristine LAGP (Figure 2B) with the large peak at 460 cm<sup>-1</sup> whereas at 0.8 V new sharp peaks at 1087 and 943 cm<sup>-1</sup> and a broad peak at 290 cm<sup>-1</sup> are observed. Spectral images at these 4 wavenumbers were created to assess the spatial heterogeneity of the LAGP decomposition products (Figure 4C). The band at 460 cm<sup>-1</sup> is assigned to the v(O-P-O) bending mode of LAGP while the peak at 290 cm<sup>-1</sup> is attributed to the phonon mode of a-Ge. Furthermore, the two new peaks at 943 and 1087 cm<sup>-1</sup> which were not observed in the single point experiment are assigned to PO<sub>4</sub> stretching in Li<sub>3</sub>PO<sub>4</sub><sup>31</sup> and pyrophosphate anion stretching in Li<sub>4</sub>P<sub>2</sub>O<sub>7</sub>.<sup>32</sup> The color intensity in the Raman images is related to the (relative) intensity of the Raman peaks in each location.

At 2.24 V, the 460 cm<sup>-1</sup> peak intensity image of the Cu/LAGP interface is relatively uniform albeit with some minor variation in the intensity, suggesting some degree of heterogeneity at the initial Cu/LAGP interface. As the potential decreases to 1.52 V, there is still no significant reaction, and the Raman images look similar. When the potential reaches 1.16 V there is a distinct decrease in the overall intensity related to the O-P-O bending mode at 460 cm<sup>-1</sup> and the emergence of several hotspots corresponding to the phonon modes of a-Ge at 290 cm<sup>-1</sup>. Th trend continues at 0.98 V where the 460 cm<sup>-1</sup> peak intensity decreases fairly uniformly across the 40x40 µm<sup>2</sup> area and the intensity of the band at 290 cm<sup>-1</sup> increases in what appears to be a very heterogenous manner. This is accompanied by emergence of a peak at 943 cm<sup>-1</sup> corresponding to a Li<sub>3</sub>PO<sub>4</sub> species which is distributed non-uniformly as well. Interestingly, there is a distinct boundary at 0.98 V which qualitatively matches well with the contrast seen in the optical image (Figure 4a, inset). At 0.80 V, the LAGP signal intensity continues to decrease reaching zero in some areas while the 290, 943, 1087 cm<sup>-1</sup> peak intensity increases implying that the phase transformation has occurred in a heterogenous manner based on the nonuniformity of the a-Ge peak intensity at 290 cm<sup>-1</sup>. Notably, the phosphate related peaks at 943 and 1087 cm<sup>-1</sup> were absent in the single point operando measurement (Figure 2,3).

Based on the Raman results, we can describe the reaction mechanism at the Cu/LAGP interface and the implications of the

observed heterogeneity. As the potential moves to ~1.6 V, direct charge transfer from the Cu electrode to Ge<sup>+4</sup> occurs to form metallic Ge<sup>0</sup> (and likely Li<sub>2</sub>O) which aggregates to form Ge nanocrystalline particles with detectable lattice phonon modes. This reaction appears to be initially confined to 6 nm region of LAGP adjacent to the Cu electrode surface estimated from the 0.016 C/cm<sup>2</sup> of cathodic charge passed from OCV to 1.0 V. At lower potentials (<0.8 V), the Ge is electrochemically lithiated to form Li<sub>x</sub>Ge phases which are mixed ion-electron conductors and can propagate the reaction zone further into the LAGP (as demonstrated by the continuous current increase toward 0 V). Lithium rich e.g., Li<sub>x</sub>Ge (1<x<3.75) amorphous and crystalline phases

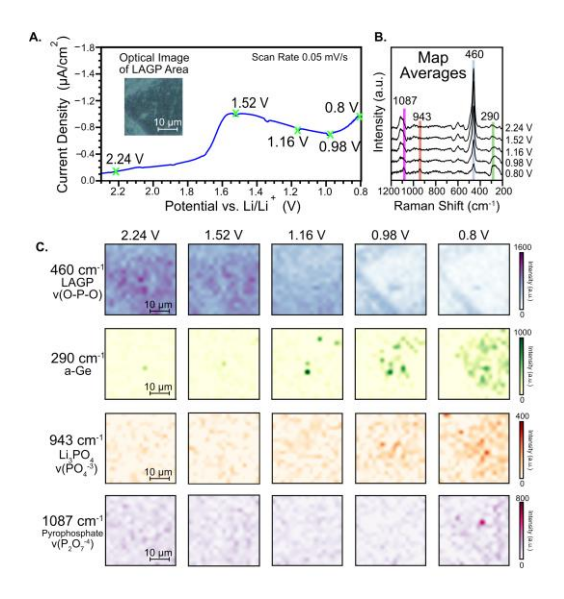


**Figure 4:** A. LSV from 2.25-0.0 V at 0.05 mV/s showing the voltages at which the mapping measurements were performed. Optical image of mapped LAGP area in inset. **B.** Average spectra of the maps from 2.24 V and 0.8 V with labelled peaks of the generated maps. **C.** Raman maps at  $459 \text{ cm}^{-1}$  (LAGP),  $290 \text{ cm}^{-1}$  (a-Ge),  $943 \text{ cm}^{-1}$  (Li<sub>3</sub>PO<sub>4</sub>) and  $1087 \text{ cm}^{-1}$  (pyrophosphate) of Cu/LAGP interface at different voltages.

are weak Raman scatterers. Therefore, they could not be observed at potentials <0.8 V. During the anodic scan electrooxidation and delithiation of the Li<sub>x</sub>Ge to Ge<sup>0</sup> occurs, as documented by the reemergence of the 290 cm<sup>-1</sup> a-Ge phonon mode. Based on the accumulated anodic charge (0.115 C/cm<sup>2</sup>), this resistive 51 nm Ge layer (assuming Li<sub>3.75</sub> Ge  $\rightarrow$  Ge) adjacent to the Cu prevents further delithiation thus trapping Li further away from the surface Cu surface as Li<sub>x</sub>Ge phases. Interestingly, Ge particles nucleate and grow within the phosphate matrix which traps Li<sup>+</sup> and forms a highly heterogeneous phase pattern on the micron-scale. It is likely that the preferred reaction and aggregation sites of Ge<sup>0</sup> and phosphates are linked with the non-uniform current density distribution due to local defects at the Cu/LAGP interface.

Based on the observed Raman images, we can identify two length scales of heterogeneity during the cathodic reactions at Cu/LAGP interface. The 10's of micron surface features where there is a clear boundary in the LAGP reaction (e.g. 0.98 V, 460 cm<sup>-1</sup>) correlates with the white and darker regions of the optical image. We investigated this surface region by AFM (**Figure S4**) and found that black region had a high root mean square (RMS) surface roughness (187.4 nm) with distinct grains typical of a polycrystalline ceramic. In contrast, the white area (more reflective area) had a much flatter topography (58 nm RMS surface roughness)

ARTICLE Journal Name

demonstrating a topographical difference between the two areas which appears to affect the rate or overpotential for interfacial decomposition. The other type of heterogeneity is linked with formation of reaction hot spots as seen in the images of a-Ge at 0.98 and 0.80 V (Figure 4c). This micron-scale heterogenous reaction pattern could originate from the wide variety of local non-uniformities on the LAGP surface e.g., surface roughness, grain boundaries and grain size variation, which could alter the local current distribution. We note that no modification of the original LAGP membranes surface was performed other than plasma cleaning to remove the carbon-containing surface layer (Figure S1).

These results highlight a major challenge in maintaining stable SSE interphases in solid-state batteries: characterization and evaluation of surface heterogeneities and their ramifications on the local current densities during operation. Heterogeneous decomposition of LAGP into distinct islands of a-Ge will result in focusing of current at the surface into regions that are rich with Ge (due to Ge's higher electrical conductivity) to form Li<sub>x</sub>Ge. The stresses built by the local volume expansion of the Li<sub>x</sub>Ge phases can exceed the failure stress of the LAGP resulting in crack formation. 17 Once cracks form during cycling, the performance deteriorates further due to broken solid-solid contacts and the resulting impedance rise. Such a catastrophic failure arises from relatively small intrinsic inhomogeneities at the solid-electrolyte interface and associated interfacial reactions. Therefore, it is important to characterize and assess these root causes of the system failure and reduce/remove them to improve the electrochemical performance and interfacial stability.

In operando Raman mapping can be a very effective tool to evaluate the presence of reaction hot spots at the solid-solid interfaces and to provide evidence that surface treatments such as polishing or interlayer deposition can effectively homogenize the interfacial current distribution. We anticipate that this methodology can be applied to a variety of SSE to evaluate the interfacial stability and electrochemical reactions at the surface with adequate temporal and spatial resolution.

This work was supported by the Assistant Secretary for Energy Efficiency and Renewable Energy, Vehicle Technologies Office, under the Advanced Battery Materials Research (BMR) Program, of the U.S. Department of Energy under Contract No. DE-AC02-05CH11231. The work at the Molecular Foundry was supported by the Office of Science, Office of Basic Energy Sciences, of the U.S. Department of Energy under Contract No. DE-AC02-05CH11231.

### Data availability

The data supporting this article have been included as part of the FSI

#### **Conflicts of interest**

There are no conflicts to declare.

### References

1 P. Albertus, V. Anandan, C. Ban, N. Balsara, I. Belharouak, J. Buettner-Garrett, Z. Chen, C. Daniel, M. Doeff, N. J. Dudney, B. Dunn, S. J. Harris, S. Herle, E. Herbert, S. Kalnaus, J. A. Libera, D. Lu, S. Martin, B. D. McCloskey, M. T. McDowell, Y. S. Meng, J. Nanda, J. Sakamoto, E. C. Self, S. Tepavcevic, E. Wachsman, C. Wang, A. S. Westover, J. Xiao and T. Yersak, *ACS Energy Lett.*, 2021, **6**, 1399. 2 A. Paolella, W. Zhu, G. Xu, A. L. Monaca, S. Savoie, G. Girard, A. Vijh, H. Demers, A. Perea, N. Delaporte, A. Guerfi, X. Liu, Y. Ren, C. Sun, J. Lu, K. Amine and K. Zaghib, *Adv. Energy Mater.*, 2020, **10**, 2001497.

3 R. DeWees and H. Wang, ChemSusChem, 2019, 12, 3713.

4 Y. Xiao, Y. Wang, S.-H. Bo, J. C. Kim, L. J. Miara and G. Ceder, *Nat. Rev. Mater.*, 2020, **5**, 105.

5 Y.-K. Sun, ACS Energy Lett., 2020, 5, 3221.

6 K. Jung, H. Shin, M. Park and J. Lee, ChemElectroChem, 2019, 6, 3842.

7 G. Homann, P. Meister, L. Stolz, J. P. Brinkmann, J. Kulisch, T. Adermann, M. Winter and J. Kasnatscheew, *ACS Appl. Energy Mater.*, 2020, **3**, 3162.

8 P. Hartmann, T. Leichtweiss, M. R. Busche, M. Schneider, M. Reich, J. Sann, P. Adelhelm and J. Janek, *J. Phys. Chem. C*, 2013, **117**, 21064.

9 M. Barj, H. Perthuis and Ph. Colomban, *Solid State Ion.*, 1983, **9**, 845.

10 B. E. Francisco, C. R. Stoldt and J.-C. M'Peko, *Chem. Mater.*, 2014, **26**, 4741.

11 M. Zhang, K. Takahashi, N. Imanishi, Y. Takeda, O. Yamamoto, B. Chi, J. Pu and J. Li, *J. Electrochem. Soc.*, 2012, **159**, A1114–A1119. 12 Y. Zhu, X. He and Y. Mo, *ACS Appl. Mater. Interfaces*, 2015, **7**, 22695

13 J. K. Feng, L. Lu and M. O. Lai, *J. Alloy. Compd.*, 2010, **501**, 255. 14 Z. Tong, Y.-M. Lai, C.-E. Liu, S.-C. Liao, J.-M. Chen, S.-F. Hu and R.-S. Liu, *ACS Appl. Energy Mater.*, 2022, **5**, 11694.

15 Y. Liu, C. Li, B. Li, H. Song, Z. Cheng, M. Chen, P. He and H. Zhou, *Adv. Energy Mater.*, , DOI:10.1002/aenm.201702374.

16 Z. Ding, J. Li, J. Li and C. An, *J. Electrochem. Soc.*, 2020, **167**, 070541.

17 L. He, J. A. S. Oh, K. Watarai, M. Morita, Y. Zhao, Q. Sun, T. Sakamoto, L. Lu and S. Adams, *Chem. Mater.*, 2021, **33**, 6841–6852. 18 W. Lei, C. Zhang, R. Qiao, M. Ravivarma, H. Chen, F. B. Ajdari, M. Salavati-Niasari and J. Song, *ACS Appl. Energy Mater.*, 2023, **6**, 4363. 19 H. Chung and B. Kang, *Chem. Mater.*, 2017, **29**, 8611–8619. 20 A. I. Inozemtseva, V. A. Vizgalov, O. O. Kapitanova, G. Panin, J. J. V. Vélez, D. M. Itkis, D. Yu. Usachov and L. V. Yashina, *J. Electrochem. Soc.*, 2020, **167**, 110533.

21 L. Sang, R. T. Haasch, A. A. Gewirth and R. G. Nuzzo, *Chem. Mater.*, 2017, **29**, 3029.

22 L. Sang, K. L. Bassett, F. C. Castro, M. J. Young, L. Chen, R. T. Haasch, J. W. Elam, V. P. Dravid, R. G. Nuzzo and A. A. Gewirth, *Chem. Mater.*, 2018, **30**, 8747.

23 B. E. Francisco, C. R. Stoldt and J.-C. M'Peko, *J. Phys. Chem. C*, 2015, **119**, 16432.

24 N. Ishiguro, T. Totsuka, H. Uematsu, O. Sekizawa, K. Yamamoto, Y. Iriyama and Y. Takahashi, *ACS Appl. Energy Mater.*, 2023, **6**, 8306. 25 A. Axelevitch, B. Gorenstein and G. Golan, *Phys. Procedia*, 2012, **32**, 1.

26 V. M. Zallocco, J. M. Freitas, N. Bocchi and A. C. M. Rodrigues, *Solid State Ion.*, 2022, **378**, 115888.

27 J. Miao, B. Wang and C. V. Thompson, *J. Electrochem. Soc.*, 2020, **167**, 090557

28 L. C. Loaiza, N. Louvain, B. Fraisse, A. Boulaoued, A. Iadecola, P. Johansson, L. Stievano, V. Seznec and L. Monconduit, *Journal of Physical Chemistry C*, 2018, **122**, 3709.

29 J. S. Peña, I. Sandu, O. Joubert, F. S. Pascual, C. O. Areán and T. Brousse, *Electrochem. Solid-State Lett.*, 2004, **7**, A278.

30 D. McNulty, H. Geaney, D. Buckley and C. O'Dwyer, *Nano Energy*, 2018. **43**. 11.

31 L. Popović, B. Manoun, D. de Waal, M. K. Nieuwoudt and J. D. Comins, *J. Raman Spectrosc.*, 2003, **34**, 77.

32 Y. Kowada, M. Tatsumisago and T. Minami, *J. Phys. Chem.*, 1989, **93**, 2147.

Page 5 of 5 ChemComm

The data supporting this article have been included as part of the Supplementary Information.

We have added the python code used and an example spectra file as part of the supporting information.

Also, we included an example of Raman data.

All experimental data are available from authors upon request.